ARTICLE OPEN

Check for updates

Photoexcitation induced magnetic phase transition and spin dynamics in antiferromagnetic MnPS$_3$ monolayer

Yinlu Gao[1,2], Xue Jiang [ID][1,2 ✉], Zhiyong Qiu [ID][2,3] and Jijun Zhao [ID][1,2 ✉]

Antiferromagnetic spin dynamics is the key issue to develop spintronic devices. We adopt ab initio nonadiabatic molecular dynamics with spin–orbit-coupling (SOC) to investigate photoinduced spin dynamics in an antiferromagnetic semiconductor MnPS$_3$ monolayer. Optical doping triggers MnPS$_3$ from Néel antiferromagnetic to ferromagnetic phase at an experimentally achievable electron–hole pair density of 1.11×10^{14} cm^{-2}. This phase transition can be ascribed to the light-induced mid-gap states of S-p orbitals, which lower the electron excitation energy and strengthen the SOC effect between S-p and Mn-d orbitals. The excited S-p electrons first decay to the mid-gap states due to p–p electron–phonon-coupling and then relax to the spin-down Mn-d orbitals via SOC. Such a dramatic relaxation process prolongs the photogenerated carrier lifetime up to 648 fs, providing an explanation for the unusual optoelectronic performance of MnPS$_3$. The reversible switching of magnetic order via optical means gives an important clue for information storage and highly efficient photocatalysts utilizing antiferromagnetic semiconductors.

INTRODUCTION

Two-dimensional (2D) magnets have blossomed into one of the most promising areas in condensed matter physics over the past years. Inspired by the successful synthesis of intrinsic 2D magnetic semiconductors, i.e., CrI$_3$ monolayer and Cr$_2$Ge$_2$Te$_6$ bilayer, scientists have vastly broadened the family of potential 2D magnets, including CrX$_3$ (X = Cl, Br), Fe$_3$GeTe$_2$, VSe$_2$, MnSe$_2$, CrSBr, and MPS$_3$ (M = Fe, Mn, Ni)[1–4]. These emerging 2D magnets provide an ideal platform for manipulating the spin at the 2D limit, leading to significant advances in low-power-consuming spintronics, quantum computing, and optical communications. Furthermore, there is a fast-growing interest in developing effective approaches to control spin structure via an electric field, mechanical strain, defect doping, molecule adsorption, magnetic field, and so on[5–8]. Among these approaches, the ultrafast laser has a distinctive advantage since it is the fastest, non-contact, and most energy-efficient way to manipulate spin.

Specifically, employing light to control the magnetic order via spin transfer or demagnetization process has attracted extensive attention. For MXenes with ferrimagnetic (FiM) order, such as Cr$_2$VC$_2$F$_2$, Mo$_2$VC$_2$F$_2$, Mo$_2$VN$_2$F$_2$, Mo$_3$C$_2$F$_2$, and Mo$_3$N$_2$F$_2$, He et al. found that the laser pulse can directly trigger a magnetic transition from FiM to transient FM within a few femtoseconds. Time-dependent density-functional theory (TDDFT) simulations revealed that the microscopic origin of the transient all-optical switching of spin order was the optically induced intersite spin transfer (OSITR) effect[9]. The optically driven magnetic phase transition has also been observed in 2D spin-liquid RuCl$_3$, where the FM phase was significantly stabilized by optical doping at a moderate electron–hole (e–h) density of 1×10^{13} cm^{-2}[10].

Besides the magnetic phase transition, a drastic change in magnetic anisotropy was achieved in the CrI$_3$ monolayer. The easy magnetization axis switches from out-of-plane to in-plane along with a large magnetic anisotropy energy (MAE)[11]. Using an ultrashort laser pulse, Dabrowski et al. demonstrated the laser-induced formation of the magnetic domain after thermal demagnetization in ultrathin CrI$_3$. They also realized helicity-dependent all-optical switches in CrI$_3$[12]. In a few-layer Fe$_3$GeTe$_2$, both magnetization orientation and amplitude of MAE can be effectively modulated by a laser pulse. The saturation magnetization and coercivity were continuously tunable and the Curie temperature was boosted to room temperature[13]. All these efforts have contributed to the spin control of ferromagnets, while spin dynamics in 2D AFM materials remain largely unexplored[14]. Compared to 2D ferromagnets, the interaction between light and 2D antiferromagnets would pave the way for optically controlling the magnetic materials with a faster timescale and promise stronger magneto-transport effects.

In this paper, we focus on the experimentally synthesized transition metal thiophosphate MnPS$_3$ monolayer as a representative AFM semiconductor[15–17]. Its spin dynamics under light illumination are investigated using the time-domain ab initio nonadiabatic molecular dynamics (NAMD) method with the inclusion of spin–orbit-coupling (SOC) within the spin-diabatic representation. Our results demonstrate that optical doping can convert the magnetic ground state of the MnPS$_3$ monolayer from AFM to ferromagnetic (FM). Accounting for the optically induced mid-gap states, both d–p–d FM superexchange and p–d SOC are strengthened. During the carrier relaxation process, the excited S-p electrons firstly relax to p orbitals by transferring their energy to the lattice through electron–phonon coupling (EPC) and then to Mn-d orbitals to recombine with the holes via SOC. These findings not only deepen our understanding of spin dynamics of 2D materials but also provide opportunities for spintronic applications of AFM semiconductors using optical switches.

RESULTS AND DISCUSSION

Structural and magnetic properties of MnPS$_3$ monolayer

As shown in Fig. 1a, b, Mn^{2+} cations in MnPS$_3$ monolayer form a honeycomb lattice with P–P dimers vertically across the center of

[1]State Key Laboratory of Structural Analysis for Industrial Equipment, Dalian University of Technology, 116024 Dalian, China. [2]Key Laboratory of Materials Modification by Laser, Ion and Electron Beams (Dalian University of Technology), Ministry of Education, 116024 Dalian, China. [3]Key Laboratory of Energy Materials and Devices (Liaoning Province), School of Materials Science and Engineering, Dalian University of Technology, 116024 Dalian, China. ✉email: jiangx@dlut.edu.cn; zhaojj@dlut.edu.cn
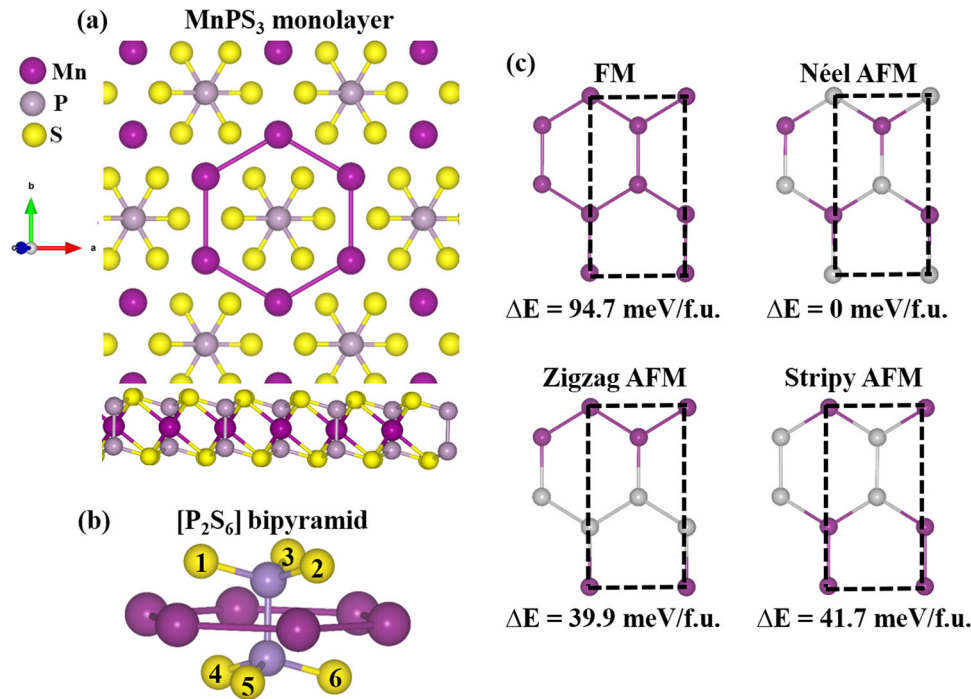
Fig. 1 Schematic structure and spin configurations. a Top and side view of MnPS$_3$ monolayer and **b** the Mn atom honeycomb lattice and centering [P$_2$S$_6$] bipyramid. **c** Spin arrangements of the FM, Néel AFM, zigzag AFM, and stripy AFM, the purple and grey balls are the spin-up and spin-down state Mn atoms, respectively. The relative energies to the Néel AFM are presented as well.

the hexagonal plane. Each P–P dimer is tetrahedrally coordinated with three S atoms to form a [P$_2$S$_6$] bipyramid. The calculated lattice parameters for MnPS$_3$ monolayer are $a = 6.15$ Å, $b = 10.66$ Å, slightly larger than the experimental values ($a = 6.08$ Å, $b = 10.52$ Å) for bulk MnPS$_3$ crystal[18]. To evaluate the magnetic ground state of 2D MnPS$_3$, four phases with different long-range magnetic orders, i.e., FM, Néel AFM, zigzag AFM, and stripy AFM, are considered using a $2 \times 1 \times 1$ supercell (Fig. 1c). Among them, the Néel AFM phase has lowest energy according to our calculations, while energy of the competing FM phase is about 94.7 meV/f.u. higher, in agreement with the previous report[19]. The Mn^{2+} ions adopt high-spin states with an on-site magnetic moment of about 4.61μ$_B$.

To further examine the magnetic ground state, exchange coupling between Mn ions has been investigated using the following Heisenberg Hamiltonian:

$$H = -\sum_{ij} J_1 \mathbf{S}_i \mathbf{S}_j - \sum_{kl} J_2 \mathbf{S}_k \mathbf{S}_l - \sum_{mn} J_3 \mathbf{S}_m \mathbf{S}_n \qquad (1)$$

where **S** is the spin magnetic moment on each atomic site, J_1, J_2, and J_3 are the exchange interactions between the first, second, and third nearest-neighbor spins, respectively. In the pristine MnPS$_3$ monolayer, all the calculated J values are negative, i.e., -0.35 meV, -0.06 meV, and -0.12 meV, respectively, which again confirm the robust AFM ground state. Due to the variance of lattice constant, bond lengths, and angles, the values of exchange parameters appear to be in disagreement with previous results that yielded $J_1 = -0.79$ meV, $J_2 = -0.04$ meV, and $J_3 = -0.23$ meV[18,20]. However, the magnitudes of the second nearest-neighbor J_2 are much smaller than J_1 and J_3, which is in reasonable agreement with previous investigations. The negative J_1 is the result of competition between direct exchange and superexchange interaction. The direct exchange originates from hopping between Mn ions, which provides a robust AFM state as the overlapped d orbitals are half-filled. Meanwhile, the angle of Mn–S–Mn bridge (83.6°) is close to 90°. According to the Goodenough–Kanamori–Anderson (GKA) rules, the superexchange through Mn–S–Mn path should belong to FM coupling[21].

Because of the short Mn–Mn distance (3.55 Å) and the high-spin state of Mn^{2+} in the MnPS$_3$ monolayer, direct AFM interaction prevails over FM superexchange. For J_2 and J_3, AFM exchange interaction derives from the super-superexchange interactions mediated by different S atoms. Specifically, J_2 involves Mn-S3···S6-Mn path in which the two S atoms are located in separate sublayers (Fig. 1b). However, in the super-superexchange channel for J_3, the two mediated S atoms are in the same sublayer (Mn-S1···S2-Mn). One can reasonably expect that hybridization of Mn-d states with S-p states within the same sublayer is significantly stronger than that between different sublayers. This accounts for the larger magnitude of J_3 in comparison to J_2 despite the longer Mn–Mn distances in the former case. Nevertheless, J_1 is larger than J_3 by a factor of 3, which ensures that the dominating exchange parameter in the pristine MnPS$_3$ monolayer is the Mn–Mn direct AFM exchange.

Effects of optical doping

Before we investigate the optical e–h bipolar doping effect on the MnPS$_3$ monolayer, the role of unipolar doping has been firstly discussed. As shown in Supplementary Fig. 1, the energy difference between Néel AFM ground state and FM state increases with the increase of both electron and hole concentrations. That is to say, the magnetic ground state of the MnPS$_3$ monolayer can be switched from Néel AFM phase to FM one at critical density for electron and hole doping of 1.07×10^{14} and 1.52×10^{13} cm^{-2}, respectively. Unlike the bilayer CrI$_3$ in which only electron doping can be used to control the magnetic phase transition[22], the FM phase can be induced by injecting either electrons or holes into the AFM MnPS$_3$ monolayer. This outstanding character indicates the possibility of controlling the magnetism simultaneously via photoexcited electron and hole.

The energy difference between the most stable Néel AFM and FM phase as a function of optical doping concentration is plotted in Fig. 2a. Once the carrier density reaches 1.11×10^{14} cm^{-2}, corresponding to 0.75 electron/hole per unit cell, the magnetic
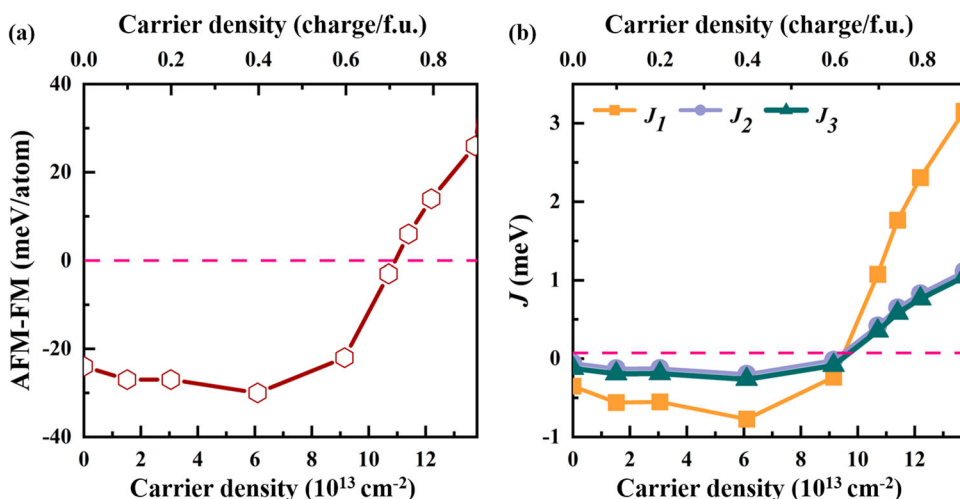
Fig. 2 The energy difference and exchange parameters vary with optical doping. a The energy difference between the Néel AFM and FM phase and **b** the calculated exchange parameters (J_1, J_2, and J_3) as a function of optical e–h doping in $MnPS_3$.

order will transition from AFM to FM. Remarkably, such critical e–h pairs density in the order of magnitude of 10^{14} cm^{-2} has already been realized experimentally with a laser pump, which ensures the achievement of stable FM $MnPS_3$ monolayer[23,24]. Moreover, mature experimental technology like the time-resolved magneto-Kerr effect also makes the detection and measurement for magnetic phase transition readily available[25]. From the variation of exchange parameters J with optical e–h pairs density (Fig. 2b), we can also obtain the same trend of AFM-to-FM transition. All J values change from negative to positive as the e–h pairs density increases. Depending on their response towards excited e–h pairs, strong competition is expected between the superexchange Mn–S–Mn FM coupling and direct Mn–Mn AFM one, which in turn leads to the magnetic order transition. Taking advantage of the photoexcited e–h pairs, the dominance of the AFM state is broken with the carrier density in the range of 1.07×10^{14}–1.11×10^{14} cm^{-2}. As is well known, photodoping is commonly accompanied by transient heating of the system. We can assume that photon transfers all their energy to the electrons since laser irradiation is an ultrafast transient process. The temperature rise of the system mainly originates from the electron–phonon interaction. After the optical pump pulse, hot electrons are created and quickly reach quasi-equilibrium with the phonon subsystem on picosecond time scales. Moreover, the phonon-specific heat capacity of magnetic insulator $MnPS_3$ is larger than the electronic-specific heat capacity. Therefore, we infer that most of the absorbed energy will reside in the phonon subsystem after the pump. After the light excitation, we obtained the internal energy of the $MnPS_3$ monolayer roughly changed by 0.24 eV using ourcalculations. Based on these assumptions, we estimated the temperature roughly increased by 35 K during the phase transition process. Luckily, this temperature is smaller than the magnetic order temperature of 78 K[17]. Details about the temperature estimation are available in the "Methods" section.

Mechanism of the opto-magnetic effect

To shed further light on the underlying mechanism of the magnetic order transition in $MnPS_3$ monolayer, both spin exchange coupling strength and spin dynamics in terms of optical excitation have been discussed. According to the anti-triangular prism of MnS_6 in $MnPS_3$ monolayer, the ideal six-coordinated octahedron crystal field splits into a single a_1 (d_{z2}) orbital and two doubly degenerate e_1 (d_{xz}, d_{yz}) and e_2 (d_{xy}, d_{x2-y2}) orbitals. From the partial density of states (PDOS) in Fig. 3a, b, the strong crystal field effect makes almost all d electrons occupying the spin-down

channel, while only few d electrons occupy the spin-up channel, which leads to the high-spin state of Mn ions. However, the optical excitation destroys the hybridization between d_{xz} (d_{xy}) and d_{yz} ($d_{x2−y2}$) orbitals of Mn atoms, as revealed by the optically doped $MnPS_3$ with 1.11×10^{14} cm^{-2} density in Fig. 3c, d. The reduced degeneracy of both e_1 and e_2 energy levels weakens the AFM interaction between neighboring Mn atoms. In addition, the lattice vibration will be perturbated during the process of system heating up. Due to the strong electron–phonon interaction, the additional electron (hole) becomes trapped and localized on S (Mn/P) atom while the surrounding lattice is distorted. The distances between the Mn–Mn bond lengths increase with the increase of the density of e–h pairs, while the distance between Mn–S decrease (Supplementary Fig. 2). The elongated distance between Mn–Mn also reduces the AFM coupling.

By comparing the electronic structures of pristine and optically e–hdoped $MnPS_3$ monolayers (Fig. 3a–d), it is found that optical pumping results in a reconstruction of conduction band edge to create localized mid-gap states in the forbidden band gap, accompanied by a remarkably inward shift of conduction band edge in $MnPS_3$. The behavior of n-type semiconductors for optically doped $MnPS_3$ means that the photoinduced electrons are more effective than holes in driving electronic phase transition. Further analysis of PDOS reveals that the mid-gap states are mainly composed of degenerate S-p_x and S-p_y orbitals, which are fully occupied in the spin-up channel. As shown in Supplementary Fig. 3, the photogenerated holes will transfer from the valence band to the mid-gap states, which results in the enhancement of FM coupling. Moreover, the additional S-p and Mn-d hybridization can be seen in the energy range 1–1.5 eV from Fig. 3c, d, which gives rise to a magnetic moment of ~0.16 μ_B on each S atom. During the process of optical excitation, part of the spin density in the spin-down channel on Mn atoms is transferred to the spin-up channel on S atoms, which will be discussed in detail later. The optical pumping induced mid-gap states and change of occupied number have also been found in previous experiments on 1T-TaS_2, 1T-$TiSe_2$, and VO_2 using time- and angle-resolved photoemission spectroscopy[26–29]. The collapse of their long-range charge order with a frozen lattice is possibly caused by the screening effect due to the creation of extra intraband electron–hole channels. Moreover, the mid-gap states created by optical doping in the $MnPS_3$ monolayer narrow the band gap from 2.34 to 1.40 eV. Therefore, the energy difference between S-$3p$ orbitals and Mn-$3d$ orbitals becomes smaller, which will facilitate carrier hopping between them by largely lowering the electron excitation energy and enhance he FM superexchange interaction.
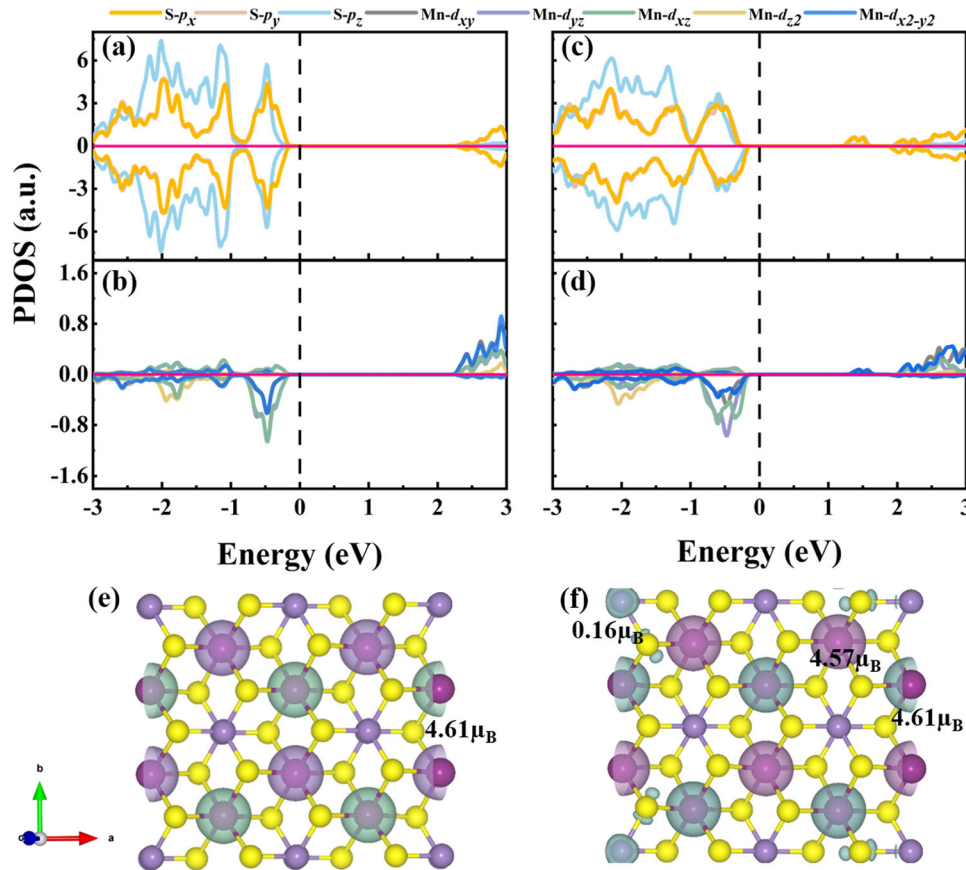
Fig. 3 Electronic properties and spin density before and after optical doping. Projected density of states of **a** S-3p and **b** Mn-3d orbitals in intrinsic MnPS$_3$ monolayer in Néel AFM state and **c**, **d** optical e–h-doped MnPS$_3$ with a density of 1.11×10^{14} cm^{-2}. The spin density **e** before and **f** after optical e–h doping. The cyan and purple balls represent spin-up and spin-down electrons, respectively. The iso-surface value was set to 0.001 eV/Bohr^3.

Consequently, the optically controlled magnetic phase transition from AFM to FM can be realized in the MnPS$_3$ monolayer.

Spin dynamic process

The dynamic response of magnetic order to the optical excitation is further investigated using the time-dependent Kohn–Sham equation-based NAMD simulations, including the spin–flip mechanism and the carrier relaxation process. Both the spin–flip and spin e–h recombination is strongly dependent on the nonadiabatic coupling (NAC) element between the key states (Fig. 4a, b). For electrons with the same spin states, the energy of photoexcited electrons will transfer to phonons directly by EPC. Meanwhile, SOC can induce a spin–flip between opposite spin states via transferring the spin angular momentum to the orbital angular momentum. In the spin diabatic representation, Fig. 4a, b provide a straight line for comparison between the EPC and SOC in the excited MnPS$_3$ at 1.11×10^{14} cm^{-2} density. The SOC is the dominant factor rather than EPC in the p–d interaction. As mentioned above, the stronger SOC offers the channels for the population transfer from the spin-down Mn-d states to the spin-up S-p states after photoexcitation, which is responsible for the magnetic phase transition. Additionally, the lowest unoccupied spin-down state is rough 2 eV higher than the valence band (Fig. 3c, d), which makes the electron hopping between spin-down d and p states through EPC even more difficult. As a result, the spin is allowed to flip in the process of light excitation. Accordingly, the magnetic order is switched from Néel AFM to FM.

In fact, EPC and SOC always compete with each other during the spin relaxation dynamics process, which synergistically determines the behavior of electrons. The initial states are S-3p orbitals above the Fermi level by about 1.7 eV for spin-up electrons (CB in Fig. 4c), while the final states are Mn-3d near the Fermi level for spin-down electrons (VB in Fig. 4c). The photoexcited S-p electrons in CB decay to the mid-gap states of the same spin states in the forbidden band, along with the reduction of electron population in Fig. 4d from 1 to 0.5. Our NAC calculations reveal that the EPC between the S-p and S-p orbitals is much stronger than the SOC, which explains why the initial S-p states prefer to relax to the mid-gap states, rather than to the spin-down S-p orbitals with closer energy levels (Fig. 3c). However, electron population analysis discloses that most of these spin-up S-p electrons finally relax to the spin-down Mn-d states (VB) to recombinant with holes, due to the larger p-d SOC. Correspondingly, the relaxation process accompanies with spin-flip from spin-up to spin-down channel.

Figure 4e shows the spin occupation during relaxation. The spin–flip finishes within a time scale of 648 fs, which suggests the FM phase can be maintained for a long time. Owing to the mid-gap states induced by photoexcitation, the excited electrons transfer their energy through EPC firstly without spin flip, and then tend to conserve the spin via SOC (Fig. 4f). This competitive process gives rise to the FM phase of long lifetime, rather than transient one, which makes the experimental realization more convenient. We have to mention that the photoexcited carrier density will decrease due to the interband charge relaxation during the spin dynamic process. The reduced carrier density may shorten the lifetime of the photo-induced FM phase, which has not been considered here. Moreover, one should note that the
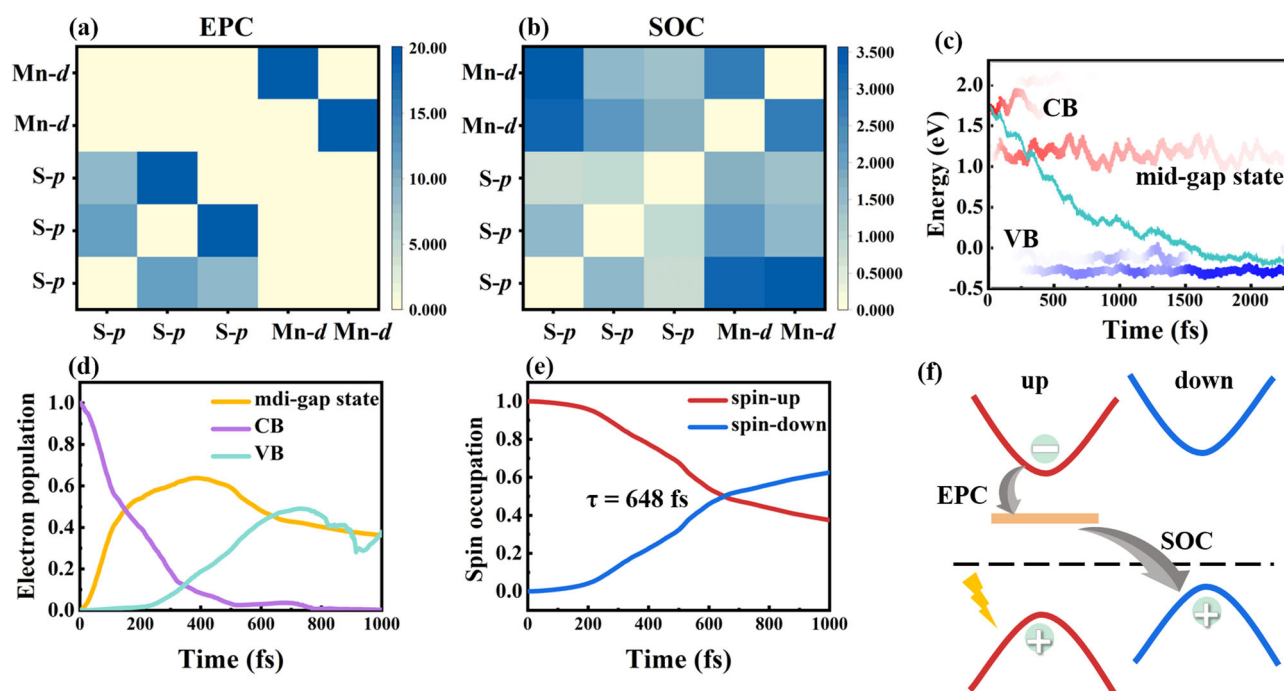
Fig. 4 Spin dynamics of spin-up and spin-down electrons in NAMD simulations. a The average electron–phonon coupling (EPC) and **b** spin–orbit coupling (SOC) between electronic states, the larger the values, the stronger the coupling. **c** Average electron energy based on the spin-diabatic representation during the dynamical process. The darker the color means the more electrons occupation of the orbital. **d** The electron population and **e** spin occupation of the excited electrons. **f** Schematic image of the photogenerated spin carrier dynamics process, the pink line represents mid-gap states in the forbidden band and the black dotted line represents the Fermi level.

SOC effect in the present system is so small that it can be treated as a perturbation in the adopted spin-diabatic representation.

The long carrier lifetime of the MnPS$_3$ monolayer also endows it a good candidate for charge separation in photovoltaics and optoelectronics. It is also well known that slower recombination is beneficial for the separation of photoexcited electrons and holes that participated in the subsequent chemical reactions such as water splitting[30]. Typically, larger bandgap and weaker EPC favor slower dynamics to avoid fast carrier recombination. Moreover, electron spin has a non-negligible impact on the control of carrier dynamics. Herein, the enhanced carrier lifetime in MnPS$_3$ is realized by the joint action of SOC and EPC upon photoexcitation. The optically driven spin state flip via SOC allows the MnPS$_3$ monolayer behaves like an indirect-gap semiconductor during the radiative recombination, simultaneously harnessing a larger carrier density of 1.11×10^{14} cm^{-2} and long lifetimes. The present findings demonstrate that the AFM MnPS$_3$ monolayer is not only attractive for spintronics but also a promising light-driven photocatalyst for environmental and energy applications. In fact, exfoliated MnPS$_3$ from the layered bulk phase has already been experimentally explored to achieve stable energy storage and conversion performances[31].

In summary, we have simulated the spin dynamics of 2D MnPS$_3$ under light illumination using the SOC-included NAMD method with spin-diabatic representation. Our computational results have shown that the intrinsic MnPS$_3$ monolayer prefers the Néel AFM phase, which can be reversely switched to the stable FM state with an experimentally achievable photoexcited e–h density at 1.11×10^{14} cm^{-2}. The mechanism for spin dynamics upon photoexcitation has been discussed based on both equilibrium exchange coupling and nonequilibrium NAC. The optical doping introduces mid-gap states that are composed of degenerate S-p orbitals and narrows the bandgap of 2D MnPS$_3$ from 2.34 to 1.40 eV. These mid-gap states decrease the energy difference between Mn-d electrons and S-p electrons, which effectively enhances the superexchange FM coupling through p–d orbital

hopping. Moreover, the reduced degeneracy in Mn-d orbitals also weakens the direct AFM interaction. According to NAC calculations, p–p orbitals interact mainly via EPC, while for p–d interaction, it is SOC. The SOC between the S-p and Mn-d states provides a spin-flipping channel between opposite spin states, which drives the magnetic phase transition from AFM to FM. During e–h recombination, the excited S-p electrons firstly relax to the mid-gap states with the same spin through the EPC channel, which effectively preserves the FM state. Since the S-p electrons relax to the spin-down Mn-d orbitals via spin flip, the FM phase decays with a timescale of 648 fs. The enhanced carrier lifetime by the magnetic phase transition may prompt MnPS$_3$ a promising photovoltaic material. Our investigation not only provides insight into the physical mechanism of optically control magnetism but also points to opportunities for the simulation of spin dynamics.

METHODS

Density functional theory calculations

The calculations were carried out within the framework of DFT, using the projector augmented wave method implemented in Vienna ab initio simulation package (VASP) code[32]. Interactions between ionic cores and valence electrons were described with the projector augmented wave (PAW) method and a cut-off energy of 500 eV[33]. The generalized gradient approximation with the PBE function was employed to describe the exchange-correlation interactions[34]. We used the Hubbard U term (5 eV for Mn) to account for strong electronic correlation effects as suggested by Dudarew et al.[35]. A 15 Å vacuum space was adopted along the perpendicular orientation to suppress the non-physical interaction between the monolayer and its adjacent imaging layer. The atomic coordinates in MnPS$_3$ monolayer were fully relaxed until the Hellmann–Feynman force and energy were <0.001 eV/Å and 10^{-6} eV, respectively. The k-point grids of $2\pi \times 0.02$ Å^{-1} were used for Brillouin-zone sampling.

In the framework of DFT, the occupation numbers of the valence and conductor bands have been manually changed to simulate the photoexcited e–h pairs. The occupied electrons in the valence bands around the Fermi level have been removed leaving holes, while the original empty conduction band is filled by excited electrons. We adopt this approach to simulate the coexistence of photoexcited electrons and holes, which has been proven as an effective way in many other systems, such as monolayer SnSe, defective diamond, and perovskites[36–38].

Methods of the temperature estimation

Following the measured specific heat, the lattice specific heat is estimated as a sum of the Debye heat $C_D(T)$ and the Einstein one $C_E(T)$ as follows[39]:

$$C_L(T) = (1-x) \times C_D(T) + x \times C_E(T) \tag{2}$$

At the low-temperature limit ($T \ll \Theta$), the lattice-specific heat is

$$C_L(T) = (1-x) \times \frac{12\pi^4}{5} Nk_B \left(\frac{\Theta_E}{T}\right)^2 + x \times 3Nk_B \left(\frac{\Theta_E}{T}\right)^2 e^{\frac{-\Theta_E}{T}} \tag{3}$$

The x value, Debye temperature, and Einstein temperature are given as 0.67, 177 K, and 422, respectively. For the monolayer sample used here, the mass is about 3.82×10^{-16} g. The calculated amount of substance is about 2×10^{-16} mol and the number of particles N in the formula above is 1.2×10^7. The internal energy change of the whole system from the DFT calculation is 0.24 eV, which gives raise a temperature increase of about 35 K.

Time-domain ab initio nonadiabatic molecular dynamics (NAMD) Methods

The photogenerated spin dynamics were simulated using SOC-included Hefei-NAMD code, which is mainly based on fewest-switches surface hopping (FSSH) combined with TDDFT[40–44]. SOC was included in the time-dependent Schrödinger equation (TDSE):

$$i\hbar \frac{\partial}{\partial t} |\psi(\mathbf{r}, \mathbf{R}, \sigma)\rangle = H^0(\mathbf{r}, \mathbf{R}(t)) + H^{soc}(\mathbf{r}, \mathbf{R}(t)) |\psi(\mathbf{r}, \mathbf{R}, \sigma)\rangle \tag{4}$$

where σ is the index of spin and H^0 is the spin-free Hamiltonian while H^{SOC} is the SOC term. The wave function is expanded by the Kohn–Sham orbitals:

$$|\psi(\mathbf{r}, \mathbf{R}, \sigma)\rangle = \sum_i |\phi_i\rangle\langle\phi_i|\psi(\mathbf{r}, \mathbf{R}, \sigma)\rangle = \sum_i c_i |\phi_i\rangle \tag{5}$$

Thus, the equation with expanding coefficients is written as

$$i\hbar \frac{\partial}{\partial t} c_i(t) = \sum_j [\langle\phi_i|H^0|\phi_j\rangle + \langle\phi_i|H^{soc}|\phi_j\rangle - i\hbar\langle\phi_i|\frac{d}{dt}|\phi_j\rangle]c_j(t)$$
$$= \sum_j [H_{ij}^0 + H_{ij}^{SOC} - i\hbar T_{ij}]c_j(t) \tag{6}$$

where T_{ij} is contributed by the EPC, which is known as the NAC in the former NAMD without SOC[43,45]. The NAMD with spin-diabatic representation was utilized in our work, where both the EPC and SOC are considered nondiagonal elements in the eigenvalues[44,46–48]. The SOC-related Hamiltonian in PAW formalism is expanded as

$$H_{ij}^{SOC} = \sum_{kl} \langle\phi_i|P_k\rangle\langle\varphi_k|H^{soc}|\varphi_l\rangle\langle P_l|\phi_j\rangle \tag{7}$$

where the $|P_k\rangle$ and $|\varphi_k\rangle$ are the projector function and all-electron partial waves, respectively, which are calculated using VASP.

The decoherence-induced surface hopping (DISH) method was used to describe the e–h recombination[49]. The Hamiltonian is related to the classical nuclear variables. The trajectory of nuclei was obtained by molecular dynamics calculations (AIMD) in advance. We used repeated velocity rescaling to heat the system to 300 K and a 2 ps adiabatic MD trajectory was achieved in the microcanonical ensemble with a 1 fs time step. Totally, 2000 structures were extracted from the 2 ps trajectories to perform the self-consistent calculation. The 150 initial configurations were selected randomly in the trajectory and 5000 NAMD trajectories were sampled for each initial structure. The initial and final states in the photoexcitation process are selected among the levels near the conduction band minimum and valence band maximum.

REFERENCES

1. Gong, C. et al. Discovery of intrinsic ferromagnetism in two-dimensional van der Waals crystals. *Nature* **546**, 265–269 (2017).
2. Huang, B. et al. Layer-dependent ferromagnetism in a van der Waals crystal down to the monolayer limit. *Nature* **546**, 270–273 (2017).
3. Jiang, X. et al. Recent progress on 2D magnets: fundamental mechanism, structural design and modification. *Appl. Phys. Rev.* **8**, 031305 (2021).
4. Guo, Y., Zhou, S. & Zhao, J. Two-dimensional intrinsic ferromagnets with high Curie temperature: synthesis, physical properties and device applications. *J. Mater. Chem. C* **9**, 6103–6121 (2021).
5. Jin, Y., Yan, M., Dedkov, Y. & Voloshina, E. Realization of the electric-field driven "one-material"-based magnetic tunnel junction using van der Waals antiferromagnetic MnPX₃ (X: S, Se). *J. Mater. Chem. C* **10**, 3812–3818 (2022).
6. Coak, M. J. et al. Emergent magnetic phases in pressure-tuned van der Waals antiferromagnet FePS₃. *Phys. Rev. X* **11**, 011024 (2021).
7. Wang, F. et al. Defect-mediated ferromagnetism in correlated two-dimensional transition metal phosphorus trisulfides. *Sci. Adv.* **7**, eabj4086 (2021).
8. Wu, X., Shen, Z., Xiao, W., Yang, J. & Song, C. Tunable band gap and transition between antiferromagnetism and ferromagnetism by surface adsorption in single-layer FePS₃. *J. Mater. Sci.-Mater. Electron.* **33**, 1871–1876 (2022).
9. He, J. & Frauenheim, T. Optically driven ultrafast magnetic order transitions in two-dimensional ferrimagnetic MXenes. *J. Phys. Chem. Lett.* **11**, 6219–6226 (2020).
10. Tian, Y., Gao, W., Henriksen, E. A., Chelikowsky, J. R. & Yang, L. Optically driven magnetic phase transition of monolayer RuCl₃. *Nano Lett.* **19**, 7673–7680 (2019).
11. Kim, J. et al. Exploitable magnetic anisotropy of the two-dimensional magnet CrI₃. *Nano Lett.* **20**, 929–935 (2019).
12. Dąbrowski, M. et al. All-optical control of spin in a 2D van der Waals magnet. *Nat. Commun.* **13**, 5976 (2022).
13. Liu, B. et al. Light-tunable ferromagnetism in atomically thin Fe₃GeTe₂ driven by femtosecond laser pulse. *Phys. Rev. Lett.* **125**, 267205 (2020).
14. Li, D. et al. Nonlinear optical properties and photoexcited carrier dynamics of MnPS₃ nanosheets. *Opt. Express* **30**, 36802–36812 (2022).
15. Brotons-Alcázar, I. et al. Molecular stabilization of chemically exfoliated bare MnPS₃ layers. *Dalton Trans.* **50**, 16281–16289 (2021).
16. Wang, F. et al. New frontiers on van der Waals layered metal phosphorous trichalcogenides. *Adv. Funct. Mater.* **28**, 1802151 (2018).
17. Ni, Z. et al. Direct imaging of antiferromagnetic domains and anomalous layer-dependent mirror symmetry breaking in atomically thin MnPS₃. *Phys. Rev. Lett.* **127**, 187201 (2021).
18. Wildes, A., Roessli, B., Lebech, B. & Godfrey, K. Spin waves and the critical behaviour of the magnetization in MnPS₃. *J. Phys.-Condens. Matter* **10**, 6417 (1998).
19. Yang, J., Zhou, Y., Guo, Q., Dedkov, Y. & Voloshina, E. Electronic, magnetic and optical properties of MnPX₃ (X = S, Se) monolayers with and without chalcogen defects: a first-principles study. *RSC Adv.* **10**, 851–864 (2020).
20. Sivadas, N., Daniels, M. W., Swendsen, R. H., Okamoto, S. & Xiao, D. Magnetic ground state of semiconducting transition-metal trichalcogenide monolayers. *Phys. Rev. B* **91**, 235425 (2015).
21. Kanamori, J. Superexchange interaction and symmetry properties of electron orbitals. *J. Phys. Chem. Solids* **10**, 87–98 (1959).
22. Huang, B. et al. Electrical control of 2D magnetism in bilayer CrI₃. *Nat. Nanotechnol.* **13**, 544–548 (2018).
23. Kim, J.-H. et al. Renormalized energies of superfluorescent bursts from an electron-hole magnetoplasma with high gain in InₓGa₁₋ₓAs quantum wells. *Phys. Rev. B* **87**, 045304 (2013).

24. Wang, J. et al. Optical generation of high carrier densities in 2D semiconductor heterobilayers. *Sci. Adv.* **5**, eaax0145 (2019).

25. Wang, C. & Liu, Y. Ultrafast optical manipulation of magnetic order in ferromagnetic materials. *Nano Converg.* **7**, 35 (2020).

26. Wegkamp, D. et al. Instantaneous band gap collapse in photoexcited monoclinic VO_2 due to photocarrier doping. *Phys. Rev. Lett.* **113**, 216401 (2014).

27. Perfetti, L. et al. Time evolution of the electronic structure of $1T-TaS_2$ through the insulator–metal transition. *Phys. Rev. Lett.* **97**, 067402 (2006).

28. Darvishi Kamachali, R. et al. Segregation-assisted spinodal and transient spinodal phase separation at grain boundaries. *npj Comput. Mater.* **6**, 1–13 (2020).

29. Rohwer, T. et al. Collapse of long-range charge order tracked by time-resolved photoemission at high momenta. *Nature* **471**, 490–493 (2011).

30. Sun, M. et al. Photo-driven oxygen vacancies extends charge carrier lifetime for efficient solar water splitting. *Angew. Chem.-Int. Ed.* **60**, 17601–17607 (2021).

31. Gusmão, R., Sofer, Z. & Pumera, M. Exfoliated layered manganese trichalcogenide phosphite ($MnPX_3$, X = S, Se) as electrocatalytic van der Waals materials for hydrogen evolution. *Adv. Funct. Mater.* **29**, 1805975 (2019).

32. Kresse, G. & Furthmüller, J. Efficiency of ab-initio total energy calculations for metals and semiconductors using a plane-wave basis set. *Comput. Mater. Sci.* **6**, 15–50 (1996).

33. Kresse, G. & Furthmüller, J. Efficient iterative schemes for ab initio total-energy calculations using a plane-wave basis set. *Phys. Rev. B* **54**, 11169 (1996).

34. Perdew, J. P., Burke, K. & Ernzerhof, M. Generalized gradient approximation made simple. *Phys. Rev. Lett.* **77**, 3865–3868 (1996).

35. Dudarev, S. L., Botton, G. A., Savrasov, S. Y., Humphreys, C. & Sutton, A. P. Electron-energy-loss spectra and the structural stability of nickel oxide: an LSDA+ U study. *Phys. Rev. B* **57**, 1505 (1998).

36. Abtew, T. A. et al. Dynamic Jahn–Teller effect in the NV^- center in diamond. *Phys. Rev. Lett.* **107**, 146403 (2011).

37. Paillard, C., Xu, B., Dkhil, B., Geneste, G. & Bellaiche, L. Photostriction in ferroelectrics from density functional theory. *Phys. Rev. Lett.* **116**, 247401 (2016).

38. Haleoot, R. et al. Photostrictive two-dimensional materials in the monochalcogenide family. *Phys. Rev. Lett.* **118**, 227401 (2017).

39. Takano, Y. et al. Magnetic properties and specific heat of MPS_3 (M=Mn, Fe, Zn). *J. Magn. Magn. Mater.* **272-276**, E593–E595 (2004).

40. Craig, C. F., Duncan, W. R. & Prezhdo, O. V. Trajectory surface hopping in the time-dependent Kohn–Sham approach for electron-nuclear dynamics. *Phys. Rev. Lett.* **95**, 163001 (2005).

41. Tully, J. C. Molecular dynamics with electronic transitions. *J. Chem. Phys.* **93**, 1061–1071 (1990).

42. Zheng, Q. et al. Ab initio nonadiabatic molecular dynamics investigations on the excited carriers in condensed matter systems. *Wiley Interdiscip. Rev.-Comput. Mol. Sci.* **9**, e1411 (2019).

43. Akimov, A. V. & Prezhdo, O. V. The PYXAID program for non-adiabatic molecular dynamics in condensed matter systems. *J. Chem. Theory Comput.* **9**, 4959–4972 (2013).

44. Zheng, Z., Zheng, Q. & Zhao, J. Spin–orbit coupling induced demagnetization in Ni: ab initio nonadiabatic molecular dynamics perspective. *Phys. Rev. B* **105**, 085142 (2022).

45. Duncan, W. R. & Prezhdo, O. V. Theoretical studies of photoinduced electron transfer in dye-sensitized TiO_2. *Annu. Rev. Phys. Chem.* **58**, 143–184 (2007).

46. Granucci, G., Persico, M. & Spighi, G. Surface hopping trajectory simulations with spin–orbit and dynamical couplings. *J. Chem. Phys.* **137**, 22A501 (2012).

47. Mukherjee, S., Fedorov, D. A. & Varganov, S. A. Modeling spin-crossover dynamics. *Annu. Rev. Phys. Chem.* **72**, 515–540 (2021).

48. Habenicht, B. F. & Prezhdo, O. V. Ab initio time-domain study of the triplet state in a semiconducting carbon nanotube: intersystem crossing, phosphorescence time, and line width. *J. Am. Chem. Soc.* **134**, 15648–15651 (2012).

49. Jaeger, H. M., Fischer, S. & Prezhdo, O. V. Decoherence-induced surface hopping. *J. Chem. Phys.* **137**, 22A545 (2012).

ACKNOWLEDGEMENTS

AUTHOR CONTRIBUTIONS

X.J. and J.J.Z. conceived the original ideas and supervised the work. Y.-L.G performed computational calculations. Z.Y.Q. joint the data discussions. Y.L.G., X.J., and J.J.Z. wrote the manuscript. All authors discussed the results.

COMPETING INTERESTS

The authors declare no competing interests.

ADDITIONAL INFORMATION

Supplementary information The online version contains supplementary material available at https://doi.org/10.1038/s41524-023-01071-y.

Correspondence and requests for materials should be addressed to Xue Jiang or Jijun Zhao.

Reprints and permission information is available at http://www.nature.com/reprints

Publisher's note Springer Nature remains neutral with regard to jurisdictional claims in published maps and institutional affiliations.